ADVANCED FUNCTIONAL MATERIALS
www.afm-journal.de

Hydrophobic and Electronic Properties of the E-MoS_2 Nanosheets Induced by FAS for the CO_2 Electroreduction to Syngas with a Wide Range of CO/H_2 Ratios

Kuilin Lv, Chao Teng, Minhao Shi, Yi Yuan, Ying Zhu, Jingrong Wang, Zhuang Kong, Xianyong Lu, and Ying Zhu**

The electrochemical CO_2 reduction reaction (CO_2RR) to produce CO and H_2 (syngas) is a promising method for clean energy, but challenges remain, such as controlling the CO/H_2 ratios required for the syngas yield. Herein, hydrophobic exfoliated MoS_2 (H-E-MoS_2) nanosheets are fabricated from bulk MoS_2 by a cost-effective ball-milling method, followed by decoration with fluorosilane (FAS). H-E-MoS_2 is a cost-effective electrocatalyst capable of directly reducing CO_2 and H_2O for tuneable syngas production with a wide range of CO/H_2 ratios (from 1:2 to 4:1). In addition, H-E-MoS_2 shows a high current density, 61 mA cm^{-2} at −1.1 V, and the highest CO FE of 81.2% at −0.9 V, which are higher than those of unmodified MoS_2. According to density functional theory calculations, FAS decoration on the surface of MoS_2 electrode can change the electronic properties of the edge Mo atom, which facilitates the rate-limiting CO-desorption step, thus promoting CO_2RR. Moreover, the hydrophobic surface of H-E-MoS_2 depressed the H_2 evolution reaction and created abundant three-phase contact points that provided sufficient CO_2. The hydrophobization of the electrode may provide an effective strategy for easily tuning the CO/H_2 ratio of syngas in a large range for the direct electroreduction CO_2 to syngas with an optimized CO/H_2 ratio.

1. Introduction

Synthesis gas (syngas), a gas mixture consisting primarily of carbon monoxide (CO) and hydrogen (H_2), is a versatile industrial feedstock for producing various hydrocarbons through the Fischer–Tropsch process.[1] The ratio of syngas is crucial for maximizing the product yield. Conventionally, syngas is predominantly produced from the gasification of solid coal and petroleum coke, or the steam reforming of natural gas, which not only require harsh conditions, but increase the consumption of fossil fuel. Owing to its abundance, availability, and nontoxicity, CO_2 can be regarded as an ideal chemical feedstock. Great effort has therefore been devoted to developing an effective strategy that can beneficially use CO_2 to produce valuable chemicals, and thereby significantly mitigate energy consumption and environmental impact. Among the advanced CO_2 conversion methods, the electrochemical carbon dioxide reduction reaction (CO_2RR) is promising since it provides a facile route for converting CO_2 to CO,[2] and other valuable chemicals.[3] The linear CO_2 molecule is extremely stable and CO_2RR is kinetically sluggish, in need of a high overpotential for conversion, which leads to low Faradaic efficiency (FE) and selectivity. Meanwhile, the simultaneous hydrogen evolution reaction (HER) is ubiquitous during CO_2RR in aqueous electrolytes under cathodic polarization.[3] Thus, there has been significant interest in the rational design and synthesis of CO_2RR electrocatalysts capable of tuning CO_2RR and HER rates for direct syngas production.[4] The direct electrochemical reduction of CO_2 to syngas would be more efficient, simpler, and faster, can be used directly in the Fischer–Tropsch process and can convert conventional electricity to chemical energy.

To date, a variety of materials have been explored for the electrochemical reduction of CO_2 into syngas, including Pd/C,[5] CdS_xSe_{1-x},[6] $Cu/(NiOH)_2$,[7] and others.[8–10] For example, Chen and co-workers[5] successfully fabricated syngas with controlled CO/H_2 ratios between 1:4 and 1:1.25 using precious metal palladium nanoparticles supported on carbon (Pd/C). The catalysis was attributed to a weakening of the binding energy for both adsorbed CO and H, caused by PdH from Pd. Zheng and co-workers[7] developed a novel ultrathin $Cu/(NiOH)_2$ hydride with a Cu(0)-enriched surface that enabled the electrochemical conversion of CO_2 and H_2O into syngas with CO/H_2 ratios of 1:9 to 9:1 at potentials ranging from −0.4 to −1.0 V (vs reversible hydrogen electrode (RHE)). Considering practical applications, therefore, there is an urgent need to develop earth-abundant and easily prepared catalysts on a large scale for

Dr. K. Lv, Dr. C. Teng, M. Shi, Y. Yuan, Y. Zhu, Dr. J. Wang, Dr. Z. Kong, Prof. X. Lu, Prof. Y. Zhu
Key Laboratory of Bio-Inspired Smart Interfacial Science and Technology of Ministry of Education
School of Chemistry
Beihang University
Beijing 100083, P. R. China
E-mail: xylu@buaa.edu.cn; zhuying@buaa.edu.cn
Prof. Y. Zhu
Beijing Advanced Innovation Center for Biomedical Engineering
Beihang University
Beijing 100083, China

DOI: 10.1002/adfm.201802339

CO_2RR into syngas. Recently, transition metal chalcogenides have been emerging as cost-effective promising electrocatalysts for CO_2RR due to their prominent catalytic features.[8–11] For instance, Asadi et al.[9] uncovered that MoS_2 with Mo-terminated edges, formed by chemical vapor deposition, exhibited superior performance in the electroreduction of CO_2 to CO, with a high FE (95%), a high current density of 60.5 mA cm^{-2} at −0.8 V (vs RHE) and a low overpotential (54 mV). Abbasi[10] reported that 5% niobium (Nb)-doped vertically aligned MoS_2 was used as a catalyst for CO_2RR, in which Nb near the Mo edge atoms could enhance CO formation by modifying the binding energies of intermediates to MoS_2 edge atoms. Ren et al.[11] fabricated an integrated 3D TiO_2@MoS_2 architecture for CO_2 electroreduction that displayed a maximum FE of 82% for CO at 0.7 V and a large partial current density of 68 mA cm^{-2}. Zhang et al.[12] demonstrated that amorphous molybdenum sulfide (MoS_X) on a polyethylenimine (PEI)-modified rGO substrate could be a highly efficient and selective electrocatalyst for the electroreduction of CO_2 to CO, which reached a maximum FE of 85.1% at 0.65 V (RHE). The PEI layer has been demonstrated to enhance the catalytic activity of the MoS_x by suppressing HER and stabilizing the CO_2 intermediate during CO_2 reduction. Moreover, Xie and co-workers[13] showed that MoSeS alloy monolayers catalyzed the conversion of CO_2 and H_2O into syngas with the highest FE (45.2% for CO and 51.3% for H_2) by regulating off-centre charge around the Mo atoms in the alloys. Theoretical calculations showed that the partially delocalized charge around Mo atoms could stabilize the COOH* intermediate and facilitate the rate-limiting CO desorption step. Notably, Zeng et al.[6] displayed novel work: constructed cadmium sulfoselenide (CdS_xSe_{1-x}) alloyed nanorods produced syngas with the widest range of the CO/H_2 ratios (from 1:4 to 4:1) by regulating the Se content from 0 to 1. Although significant progress has been made in CO_2 electroreduction, cost-effective and sustainable syngas production with a broad H_2/CO ratio for optimum production remains a significant challenge for practical applications. Moreover, understanding the exact mechanism for CO_2 electroreduction toward the valuable products is widely desirable.

Here, inspired by the superhydrophobic properties of electrodes with enhanced catalytic performance, we developed a hydrophobic exfoliated MoS_2 (H-E-MoS_2) nanosheet electrode for CO_2RR, fabricated by a simple refloating method of the exfoliated MoS_2 (E-MoS_2) nanosheets on glassy carbon electrodes, followed by the decoration of fluorosilane (FAS) on the surface of the electrode to fabricate a hydrophobic surface. The large-scale E-MoS_2 nanosheets with a high concentration (6.2 mg mL^{-1}) were directly fabricated from bulk MoS_2 by a facile, cost-efficient, and scalable ball-milling method,[14] which provides an opportunity for their practical application. After decoration with FAS, the H-E-MoS_2 nanosheets displayed a hydrophobic property with a water contact angle (CA) of 135.6° ± 1.9°. Here, all the products were CO and H_2, as observed by glass carbon (GC). The H-E-MoS_2 attained the highest FE (81.2% for CO production) at −0.9 V (vs RHE) in EMIM-BF_4 aqueous solution (94 mol% water), significantly larger than that for E-MoS_2 (41.2%) and other reported analogues.[5,6,13] Note that the H-E-MoS_2 electrode produced syngas with tuneable CO/H_2 ratios between 1:2 and 4:1 by controlling the potential, which is a greater range than that of E-MoS_2. Moreover, the HER was obviously suppressed even at a potential of −1.1 V due to the hydrophobicity of the electrode. To verify these results, we performed density functional theory (DFT) calculations to investigate the CO_2RR performance and HER activity on E-MoS_2 and H-E-MoS_2 surfaces. The calculation results showed that the FAS decoration of H-E-MoS_2 could change the electronic properties of the MoS_2 layer, which effectively decreased the energy barrier (0.72 eV, compared to 1.32 eV for E-MoS_2) of the electrode, which may suppress hydrogen evolution and also bring sufficient CO_2 to the surface of the electrode, thereby enhancing CO_2 electroreduction to syngas and broadening the H_2/CO ratio. The work presented a facile, low-cost, and effective strategy for the rational design of catalysts for the electroreduction of CO_2 to syngas.

2. Results and Discussion

2.1. Preparation and Characterization of Bulk-MoS_2 and E-MoS_2

The few-layer E-MoS_2 nanosheets were fabricated by high-energy ball milling of bulk MoS_2 powder dispersed in *N*-vinyl pyrrolidone (NVP) with an initial concentration of 16 mg mL^{-1}, as illustrated in Figure S1 of the Supporting Information. The NVP was used as a solvent because its surface free energy is very close to that of MoS_2,[15] so the MoS_2 sheets could be easily exfoliated to obtain a maximal concentration by ball milling with a large zirconium oxide (ZrO_2) ball (2 mm diameter) and a small ZrO_2 ball (0.2 mm diameter). After exfoliation for 18 h, the dark green colored dispersion was centrifuged at 550 rpm (centrifugation force 30 N) for 45 min to remove unexfoliated MoS_2. As shown in **Figure 1**A, large-volume E-MoS_2 nanosheet dispersions were obtained, indicating that ball-milling is a well-established industrial grinding technique for the exfoliation of 2D layered materials. The concentration of the as-prepared E-MoS_2 dispersion was calculated to be 6.2 mg mL^{-1}, and the yield was as high as 50.7%, much higher than what has been obtained by shear exfoliation of an MoS_2 dispersion (C = 0.5 mg mL^{-1}, yield = 1%),[16] ultrasonic exfoliation of an MoS_2 dispersion (C = 0.3 mg mL^{-1}, yield = 30%),[12] and other techniques[17–21] (Figure S2, Supporting Information). Moreover, the liquid exfoliation process (18 h) was faster than ultrasonic exfoliation (usually more than 100 h).[18] The dilute E-MoS_2 dispersion displayed an obvious Tyndall effect (Figure 1B), suggesting the successful exfoliation of the bulk material. We deduced that the bulk MoS_2 particles were fragmented and exfoliated to form the small and thin MoS_2 nanosheets by compression and shear forces of the rotating ZrO_2 balls during the milling process,[22] as demonstrated in Figures S3 and S6 of the Supporting Information.

The morphology of the E-MoS_2 was characterized by scanning electron microscopy (SEM), transmission electron microscopy (TEM), high-resolution TEM (HRTEM), and atomic force microscopy (AFM). The TEM image of the E-MoS_2 (Figure 1C) indicated a thin nanosheet with a length of 583 nm and crimp at the edge. Its elemental mapping showed a homogeneous distribution of sulfur and molybdenum, confirming its chemical composition. Figure 1D shows that the E-MoS_2 appeared to be

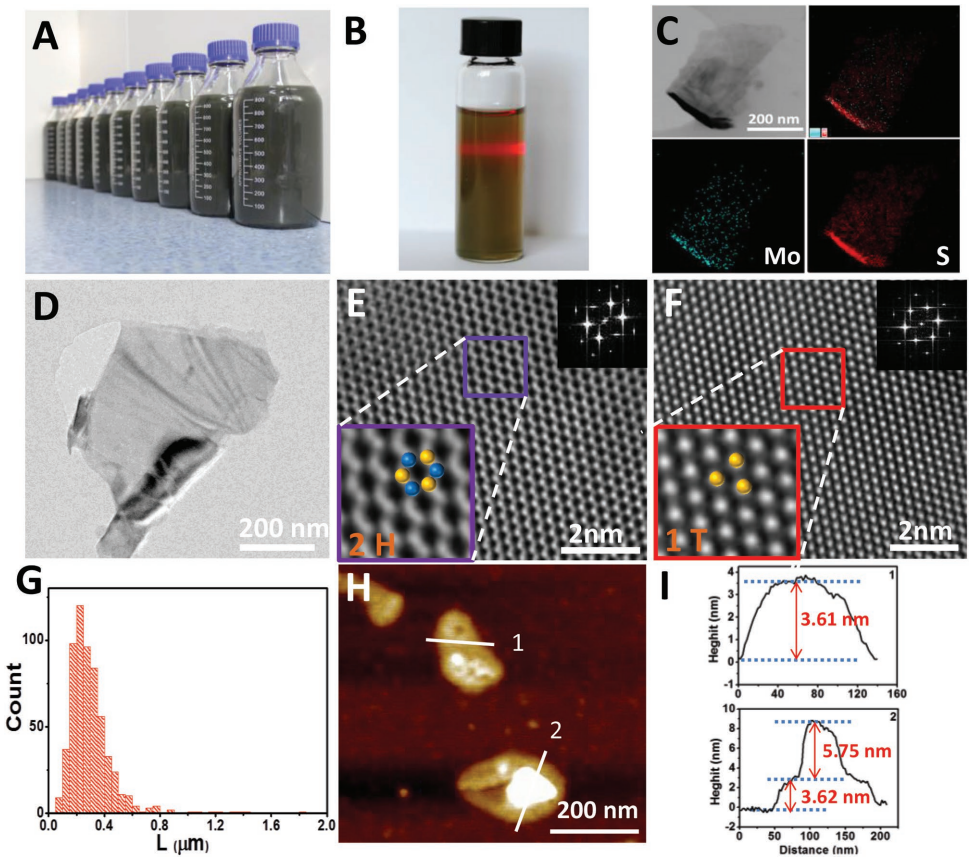

Figure 1. A) Digital photo of the exfoliated MoS_2 (E-MoS_2) nanosheets in NVP with a concentration of 3 mg mL^{-1} after ball milling. B) Tyndall effect of the diluted E-MoS_2 dispersion. C) TEM image of E-MoS_2 nanosheet and corresponding EDX maps, showing clearly the homogeneous distribution of Mo and S. D) HRTEM image of an E-MoS_2 nanosheet. E,F) Higher magnification HRTEM images of an E-MoS_2 nanosheet, showing atomic-resolution structural information, and their corresponding fast Fourier transforms (FFTs). (Insets show the 2H and 1T phases in E and F, respectively.) G) Size distribution of E-MoS_2 nanosheets as counted by TEM. H) AFM image of E-MoS_2 nanosheets. I) The corresponding height profiles; numbers 1 and 2 in (I) correspond to numbers 1 and 2 in (H), respectively.

an ultrathin layer, hundreds of nanometers in its lateral dimension, indicating that bulk MoS_2 has been efficiently exfoliated into few-layer nanosheets. The irregular shape of the exfoliated MoS_2 nanosheets was probably associated with the shear stress of the ball during the exfoliation process. The HRTEM images (Figure 1E,F) and fast Fourier transform (inset) showed that the E-MoS_2 layers were made of two clearly distinct structural domains consisting of a 1T (trigonal) phase and a 2H (hexagonal) phase, and the magnified images of selected regions further confirmed the coexistence of both 1T and 2H phases. The size of E-MoS_2 (the longest dimension) was statistically counted in TEM images of 606 flakes, revealing that the length of E-MoS_2 was in the range of 85 nm to 1.8 μm and the average length was 228 nm (Figure 1G). The E-MoS_2 nanosheets were investigated by AFM. A previous study reported that the theoretical thickness of a monolayer of MoS_2 was in the range of 0.9–1.2 nm.[23] As shown in AFM images of Figure 1H and I, two E-MoS_2 nanosheets were stacked on each other, and the thickness of the nanosheets was measured to be 3.61–5.75 nm, corresponding to 3–5 layers of MoS_2, which is consistent with the TEM results.

The molecular structure of E-MoS_2 was analyzed by X-ray diffraction spectroscopy (XRD), Raman spectroscopy and X-ray photoelectron spectroscopy (XPS). Comparing the XRD patterns of the bulk MoS_2 powder and E-MoS_2 nanosheet (**Figure 2**A), we found that the (103) and (008) diffraction peaks of E-MoS_2 decreased sharply, indicating the generation of few-layered MoS_2 nanosheets.[23] The (002) peak became broad, indicating the expansion of the interlayer distance and the relatively small size of E-MoS_2.[24] Raman spectra of bulk MoS_2 and E-MoS_2 excited by a 532 nm laser displayed approximate resonant peaks at 282, 376, 402, and 450 cm^{-1}, which arose from E^1_g and E^1_{2g} and A_{1g}, as well as the longitudinal acoustic phonon mode of 2H-MoS_2, as given in Figure 2B.[25] Raman spectra also showed peaks at 223 and 335 cm^{-1} which were ascribed to the 1T-MoS_2 phase.[26] The peak centered at 335 cm^{-1} for E-MoS_2 nanosheets showed a slight increase in intensity. It can be speculated that both the bulk MoS_2 and E-MoS_2 had a mixture of 1T and 2H phases, but the ratio of 1T- to 2H-MoS_2 in E-MoS_2 increased by ball milling. The carbon vibration at 1500 cm^{-1} was not observed, indicating there were no carbon impurities in E-MoS_2 (Figure S5, Supporting Information). As shown in the magnified Raman spectra of Figure 2C, the bulk MoS_2 had two peaks at 374.1 (E^1_{2g}) and 401.9 cm^{-1} (A_{1g}), while E-MoS_2 displayed corresponding peaks at 376 and 401.2 cm^{-1}. The corresponding frequency differences between the E^1_{2g} and A_{1g} modes were

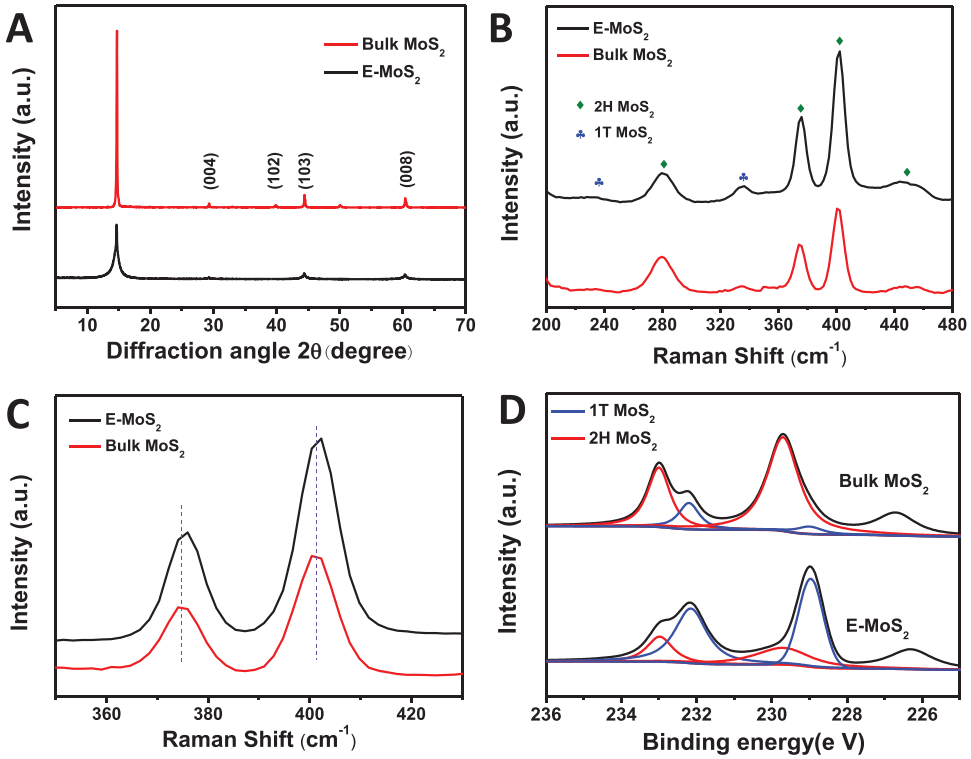

Figure 2. A) XRD patterns of bulk MoS_2 and E-MoS_2. B) Raman spectra for bulk MoS_2 and E-MoS_2 recorded using a 532 nm laser. C) Magnified Raman spectra for bulk MoS_2 and E-MoS_2; the obvious shift of peaks (E^1_{2g} and A_{1g}) indicate the decrease in the number of layers. D) XPS spectra of bulk MoS_2 and the E-MoS_2. The 1T and 2H phases of MoS_2 in the Mo 3d spectrum are indicated by the blue and red curves, respectively.

calculated to be 25.2 cm^{-1} for E-MoS_2 and 27.8 cm^{-1} for bulk MoS_2, indicating that the thickness of the MoS_2 had been significantly reduced.[27] The XRD and Raman spectra of bulk MoS_2 and E-MoS_2 thus confirmed that few-layered MoS_2 nanosheets were successfully produced. Moreover, the XPS pattern distinguished clearly the 2H and 1T phases of bulk MoS_2 and E-MoS_2 (Figure 2D); the content of 1T phase in bulk MoS_2 and E-MoS_2 were calculated to be ≈12% and 69%, respectively. Hence, we presume that a high-energy shear effect may have induced the partial structural transformation of MoS_2. It is well known that the 2H phase of MoS_2 is semiconducting in nature, while the 1T phase is metallic.[27] Previous studies have verified that the excellent catalytic activity of MoS_2 mainly derived from an increase in edge-exposed sites and the existence of the 1T phase, which facilitated electron transfer from the electrode to the active edges.[26,28] It is reasonable to assume that the high content of 1T-MoS_2 in E-MoS_2 may provide significant performance for the electroreduction of CO_2 to syngas.

2.2. CO_2 Electroreduction on E-MoS_2 and H-E-MoS_2 Electrodes

An E-MoS_2 nanosheet electrode was loaded on a 1 × 2 cm^2 area of GC without using any binder; instead, it picked up the assembled film floating on the surface of water. To get complete modification by FAS, E-MoS_2 was first treated by plasma to produce hydrophilic functional groups on E-MoS_2 nanosheets that would react with FAS during chemical vapor deposition (CVD, Figure S7, Supporting Information). Modification by CVD produced (H-E-MoS_2) nanosheets, which were used as a working electrode for the electroreduction of CO_2 to produce syngas. SEM imaging and elemental mapping (Figure S8, Supporting Information) indicted that the H-E-MoS_2 electrode had stacked 3D structures and a homogeneous distribution of Mo, S, and F elements, indicating FAS coverage on the E-MoS_2 nanosheets (Figure S8, Supporting Information). The chemical composition of H-E-MoS_2 was further revealed by XPS, XRD, and Raman spectra (Figures S9B and S10, Supporting Information). The XPS spectra indicated that the surface of H-E-MoS_2 was composed of Mo, S, C, Si, O, and F elements, indicating that FAS was successfully deposited on the surface of E-MoS_2 (Figure S9B, Supporting Information), in agreement with previous elemental mapping results. In addition, no obvious change in the crystal structure of E-MoS_2 before and after surface modification could be observed, as verified by XRD and Raman patterns. These results show that the FAS film deposited on the surface of H-E-MoS_2 did not change the structure or composition of the 1T and 2H phases of E-MoS_2. Figure S11 of the Supporting Information gave water and air bubble CA on the surfaces of the E-MoS_2 and H-E-MoS_2 electrodes in air and underwater, respectively. The E-MoS_2 electrode showed hydrophilic (water CA of 23.5° ± 2.5°) and superaerophobic (air bubble CA of 162.8° ± 1.1°) properties, while the H-E-MoS_2 electrode showed hydrophobic (water CA of 135.6° ± 1.9°) and aerophilic (air bubble CA of 65.6° ± 1.5°) properties underwater. To assess the CO_2 electroreduction performances for syngas production, linear sweep voltammetry (LSV) measurements were performed in a CO_2-saturated EMIM-BF_4 solution

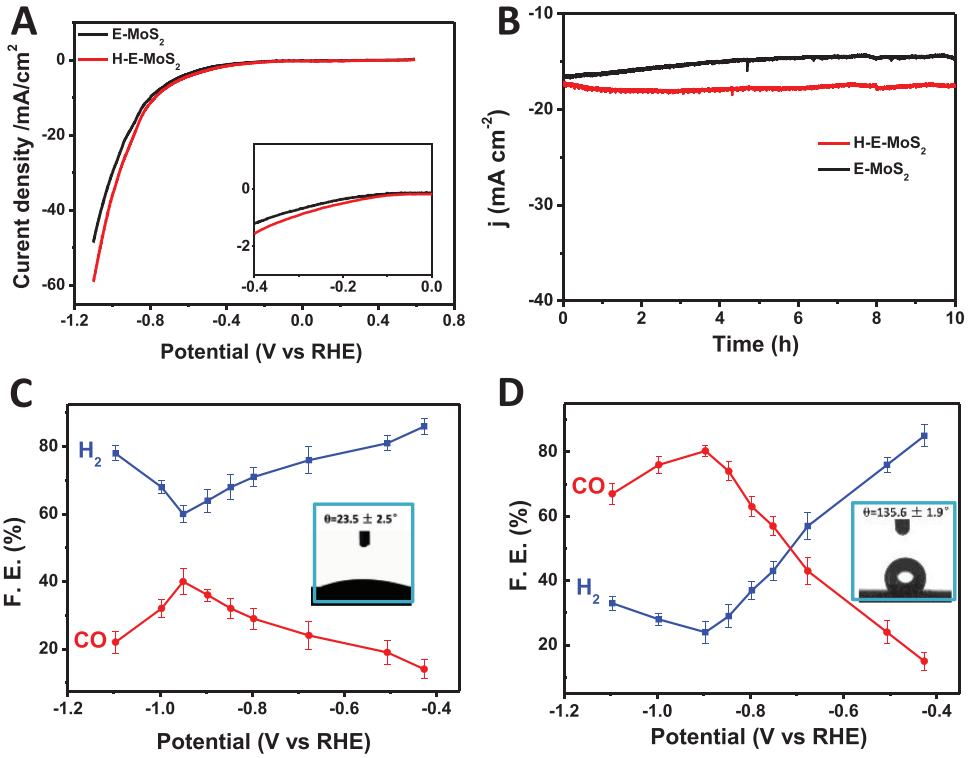

Figure 3. A) LSV curves for E-MoS_2 and H-E-MoS_2 electrodes at a sweep rate of 0.02 V s^{-1} in a CO_2 environment. B) The electrochemical stability test results of E-MoS_2 and H-E-MoS_2 catalysts at –0.8 V versus RHE in EMIM-BF_4 solutions (94 mol% water), showing negligible loss in current density even after 10 h. C) CO and H_2 Faradaic efficiency (FE%) at different applied potentials for E-MoS_2 catalysts, the inset is a photo of a water droplet on the surface of E-MoS_2, showing its hydrophilicity. D) CO and H_2 FE% at different applied potentials for H-E-MoS_2 catalysts, the inset is a water droplet on the surface of H-E-MoS_2, showing its hydrophobicity.

(94 mol% water) at a 20 mV s^{-1} scan rate (**Figure 3**A). The applied voltage was swept from 0.5 to –1.1 V versus an RHE (in the present study, all potentials are reported with respect to RHE). It is known that the equilibrium potential for the reduction of CO_2 to CO is –0.11 V. The onset potentials for CO_2 reduction with the E-MoS_2 and H-E-MoS_2 electrodes were measured to be –0.3 and –0.24 V, respectively, thus suggesting a very low overpotential (190 mV) for CO formation on a H-E-MoS_2 electrode, and less than that of E-MoS_2. In a N_2-deaerated atmosphere (Figure S12C, Supporting Information), a current that was entirely attributable to the HER was observed from –0.48 and –0.5 V for E-MoS_2 and H-E-MoS_2, respectively. Importantly, the H-E-MoS_2 electrode exhibited a significantly high current density (61 mA cm^{-2}) at –1.1 V, which was higher than that of E-MoS_2 nanosheets (48 mA cm^{-2}) and previous reports.[5,6,11] Moreover, electrochemical stability is an important criterion to assess the suitability of an electrocatalyst for practical applications. Thus, chronoamperometric responses were performed at –0.8 V for 10 h in a CO_2-saturated EMIM-BF_4 aqueous electrolyte (94 mol% water). As shown in Figure 3B, the total current density on the H-E-MoS_2 electrode showed long-term stability, while the total current density on the E-MoS_2 electrode displayed a slow decay during the reduction process. We deduced that, therefore, the electrochemical performance of CO_2 reduction on H-E-MoS_2 could be boosted by making the electrodes hydrophobicity, and FAS on an electrode could improve its electrochemical stability. The FEs for the formation of CO and H_2 were calculated at a potential range from –0.3 to –1.1 V on H-E-MoS_2 and E-MoS_2 electrodes, as shown in Figure 3C,D. In our work, CO and H_2 were the dominant products observed by GC; no liquid products could be detected by NMR. The CO/H_2 ratio could be tuned by changing the wettability of the electrode and the applied potential. For H-E-MoS_2 nanosheets, which have a hydrophobic surface, the FE of CO production increased with decreasing applied potential and reached a maximum of 81.2% ± 1.8% at –0.9 V, larger than that for CO production using E-MoS_2 (41.2% ± 1.7%). Shifting to high potential, the FE of CO decreased to 65.2% ± 2.9% at –1.1 V. By contrast, the FE of H_2 production was ≈77.5% ± 1.3% at –0.5 V, decreased to 18.8% ± 2.8% at a potential of –0.9 V, and then rose again to 34.3% ± 1.9% at –1.1 V. Moreover, even if the potential shifted to more negative values, the HER activity on H-E-MoS_2 was still obviously suppressed: the FE of H_2 decreased by 46% at –1.1 V. As a result, the CO/H_2 ratio of the syngas on the H-E-MoS_2 electrode varied from 1:2 to 4:1 as the potential ranged from –0.6 to –1.1 V, compared with that of the E-MoS_2 electrode between 1:4 and 1:1.5. Taken together, the H-E-MoS_2 electrode with the hydrophobic surface successfully provided enhanced CO_2RR performance and a broadened CO/H_2 ratio in the syngas by controlling the surface wettability. Compared with the CO_2 electroreduction performance of E-MoS_2, the CO Faradaic efficiency, the onset potentials and the CO/H_2 ratio on bulk MoS_2 were measured (Figures S12A,B and S13A, Supporting Information). The bulk-MoS_2 electrode attained a

maximum FE of 19.8% at –0.9 V, which was much lower than that of E-MoS_2 (41.2%) at same potential. The onset potential of CO_2 reduction for the bulk-MoS_2 and E-MoS_2 electrodes was measured to be at –0.43 and –0.30 V (vs RHE), suggesting a lower overpotential for CO formation on E-MoS_2 than that on bulk-MoS_2. Moreover, the CO/H_2 ratios at different potentials with different concentrations of EMIM-BF_4 aqueous electrolyte on bulk-MoS_2 are much lower than those on the E-MoS_2 electrode. Therefore, we proposed that the E-MoS_2, with high content of 1T-MoS_2, may provide an improved performance for the electroreduction of CO_2 to syngas. Moreover, to consider the effect of plasma, the CO formation FEs were measured before and after plasma treatment of E-MoS_2, as given in Figure 3C and Figure S14 (Supporting Information). It is noted that no obvious difference could be observed. This result indicated that plasma surface treatment improved FAS binding performance but did not affect CO_2 electroreduction activity.

In addition, to understand the role of the concentration of ionic liquids (ILs), the CO/H_2 ratios in syngas from the electrochemical reduction of CO_2 on the E-MoS_2 and H-E-MoS_2 electrodes at different potentials were obtained at different concentrations of EMIM-BF_4 aqueous electrolyte, as seen in Figure S13B,C of the Supporting Information. Syngas production on both the E-MoS_2 and H-E-MoS_2 electrodes reached the highest CO/H_2 ratios in 94 mol% water and 6 mol% EMIM-BF_4 aqueous solution. It has been said that EMIM-BF_4 creates protons due to the easily hydrolyzing behavior of EMIM-BF_4.[9] According to previous reports,[9,29] the concentration of protons (H^+) is the rate-determining part of the CO_2 electroreduction reaction; the maximum rate of CO_2 reduction could be obtained at the lowest pH value among different EMIM-BF_4/H_2O systems. In our work, a similar result was achieved in 6 mol% EMIM-BF_4, due to its lowest pH value (4.24, Table S6, Supporting Information). It was worth noting that all CO/H_2 ratios in syngas on the H-E-MoS_2 electrode were higher than those on the E-MoS_2 electrode at the different potentials and different concentrations of aqueous EMIM-BF_4. These results indicated that H-E-MoS_2 showed an enhanced CO_2RR activity, but notably suppressed HER activity, even if the potentials were more negative in the EMIM-BF_4 aqueous electrolyte. To understand the kinetics of CO_2RR on E-MoS_2 and H-E-MoS_2, Tafel analysis was performed on the CO partial current density. A lower magnitude of the Tafel slope for CO production is desirable, because this would indicate faster kinetics for CO formation.[30] The Tafel slope at ≈118 mV dec^{-1} suggested that single-electron transfer was the chemical rate-determining step.[6] Tafel plots on the E-MoS_2 and H-E-MoS_2 electrodes presented good linearity with slopes of 197.7 and 103.5 mV dec^{-1}, respectively (**Figure 4**). Therefore, it is clear that CO formation on the H-E-MoS_2 electrode had a faster rate than that on the E-MoS_2 electrode and single-electron transfer was the chemical rate-determining step.

2.3. DFT Calculations and Reaction Mechanism of CO_2RR

To deeply evaluate this reaction mechanism in the enhanced CO_2 electrocatalytic performance on the hydrophobic H-E-MoS_2 electrode, DFT calculations were performed on the CO_2RR and

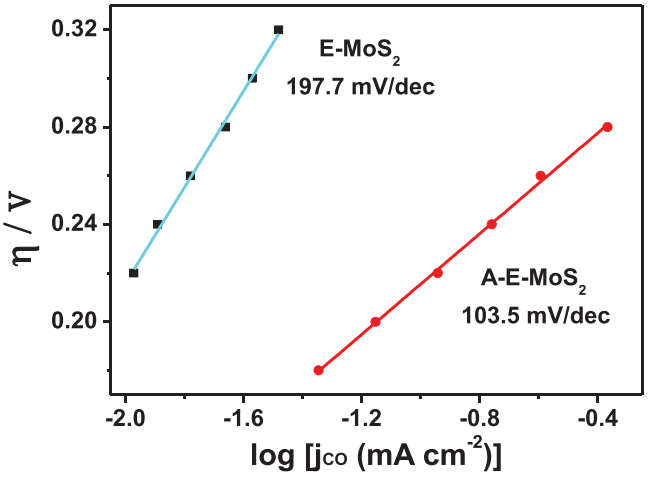

Figure 4. Tafel plots for CO production on the E-MoS_2 (blue) and H-E-MoS_2 (red) electrodes in EMIM-BF_4 solutions (94 mol% water).

HER processes. The energy profile is shown in **Figure 5**B, in which black and red lines correspond to E-MoS_2 and H-E-MoS_2, respectively. Our calculation results show that the adsorption of HOCO* and CO* on these two electrodes was exothermic, and the CO* desorption step on E-MoS_2 was a highly endothermic process (ΔG = 1.32 eV, black line in Figure 5B) and the rate-limiting step in CO_2RR on E-MoS_2. Comparing the two lines in Figure 5B, it can be found obviously that the formation of HOCO* on H-E-MoS_2 was slightly easier than it was on E-MoS_2 (0.55 eV vs 0.60 eV, Table S3, Supporting Information). However, the real rate-determining step (the desorption of CO*) had ΔG of 0.72 eV on H-E-MoS_2 (red line in Figure 5B) which was much lower than ΔG of 1.32 eV on E-MoS_2; this could be verified well by the elongation of the C—Mo bond (see Figure S17, Supporting Information), hence weakening the adsorption strength of CO with the Mo atom on H-E-MoS_2 was the real factor to promote the catalytic activity of H-E-MoS_2 in CO_2RR. Similar results were also reported in previous studies with vertically aligned MoS_2 and Nb-doped vertically aligned MoS_2 (MoS_2-Nb) as catalysts for CO_2RR.[10] Meanwhile, for the HER performance, Figure 5C showed that the ΔG for the desorption of H* on H-E-MoS_2 was slightly smaller than that on E-MoS_2. This little change could have almost no effect on overall activity of CO_2RR. To gain deep insight into the CO formation mechanism on H-E-MoS_2, we systematically investigated the process of CO_2RR on its surface (Figure 5A). The Mo atoms at the H-E-MoS_2 nanosheet edges with high activity were the catalytic sites in CO_2RR. First, the CO_2 combined with a proton–electron pair ($H^+ + e^-$) and adsorbed on the single Mo atom, forming adsorbed HOCO*. The HOCO* intermediate automatically reached a more stable configuration, where HOCO* bonded with the two neighboring Mo atoms (Figure S16, Supporting Information), which subsequently produced CO* by consuming another proton–electron pair ($H^+ + e^-$). Due to the smaller desorption energy of CO*, the adsorbed CO* intermediate could more easily desorb off from the catalytic sites to form free CO molecules. The catalytic activity was promoted by accelerating the rate-limiting step (desorption of CO*). The exoergic formation of H* in the CO_2RR process would reduce the

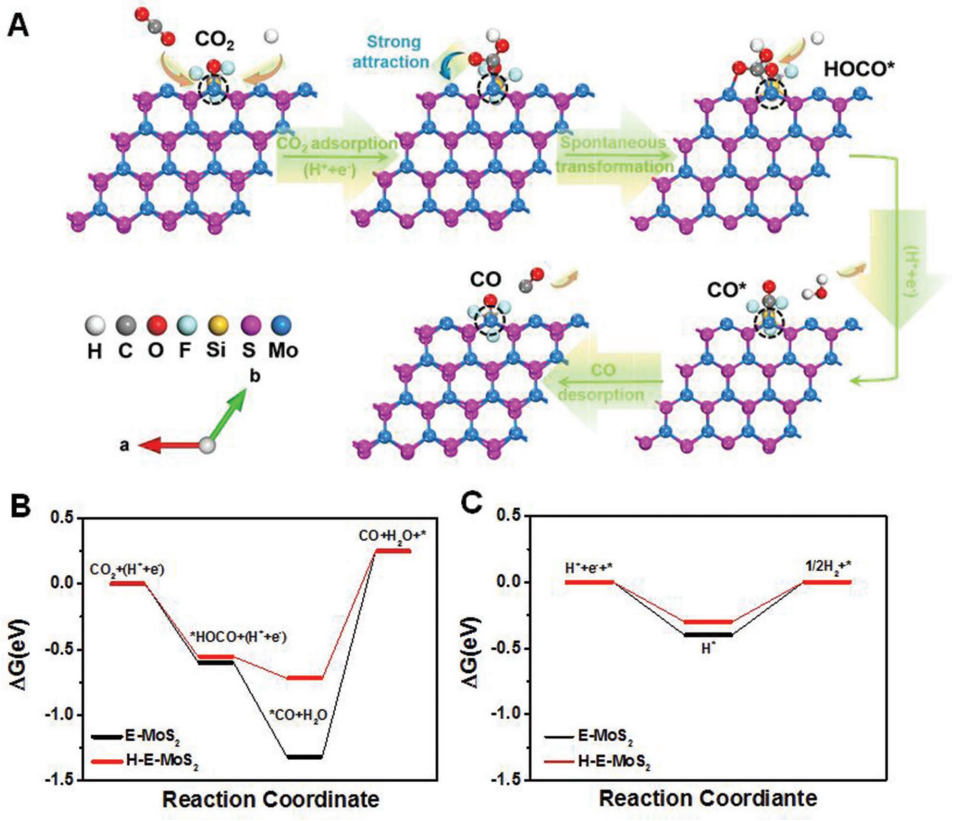

Figure 5. A) Schematic representation of CO formation mechanism on the H-E-MoS_2 monolayers. The atoms in the dashed circle are the catalytic sites (Mo atoms). Calculated free energy diagrams for B) CO_2 electroreduction to CO and C) the hydrogen evolution reaction (HER).

number of active sites and further result in the low CO formation FE.[31,32] Through DFT calculations, we found that the relative Gibbs free energy of H* on H-E-MoS_2, ΔG (H*) = –0.30 eV, which was less negative than that on E-MoS_2 (–0.41 eV), suggesting that there could be more active sites to release for CO_2RR on H-E-MoS_2. In addition to that, comparing the first step of CO_2RR with the adsorption of H, it can be found that on H-E-MoS_2, ΔG (HOCO*) (–0.56 eV) was ≈0.26 eV larger than ΔG (H*) (that on E-MoS_2 was only 0.15 eV), which indicates that the adsorption of HOCO* would be more competitive than H* adsorption. At the same time, the desorption of CO on H-E-MoS_2 decreased (only 0.70 eV) compared to that on E-MoS_2 (>1.0 eV). As a result, the FE for CO formation was improved on H-E-MoS_2. Recently, moreover, Xie et al.[33] synthesized a fluorine-interlayer-doped carbon catalyst that enabled highly selective CO_2-to-CO conversion with a high FE (89%) for CO at the first time. The result demonstrated that fluorine dopant inserted between the graphite layers could induce positive charge density and asymmetrical spin into the neighboring carbon atoms, resulting in stronger adsorption of HOCO* and better suppression of HER, leading to superior electrocatalytic performance toward CO_2RR.[33] Accordingly, we proposed that FAS decoration on the surface could create similar effects on the H-E-MoS_2 due to the strong electronegativity of F, resulting in an improved CO FE compared to E-MoS_2.

To evaluate the effect of hydrophilic and hydrophobic properties on CO_2RR, further DFT calculations were carried out to determine the free energy changes for HER on the E-MoS_2 monolayers under H_2O and CO_2 environments, respectively (**Figure 6**A). Here, the H_2O and CO_2 environments were used to simulate hydrophilic E-MoS_2 and hydrophobic H-E-MoS_2, respectively, and simplify the DFT calculations. We think that it is a reasonable simulation, due to the inherent properties of hydrophilic and hydrophobic electrodes, as demonstrated in Figure 6B,C. Our calculated results show that the abundant CO_2 environment of the hydrophobic electrode could increase the energy barrier of H* desorption to suppress the catalytic activity of HER, compared with the water environment of the hydrophilic electrode, which is consistent with the shorter H—Mo bond under the CO_2 environment (Figure 6A). Under the H_2O environment, as shown in Figure 6B,C, the H—Mo bonds of MoS_2 were 1.75 Å, longer than those in the CO_2 environment (1.73 Å), which means that the H* desorption could happen easier under the H_2O environment for H_2 desorption, thus facilitating HER. Thereby, we deduce easily that hydrophobic H-E-MoS_2 can depress HER, and thereby improve CO_2RR performance. In addition, to further illuminate the role of the hydrophobic surface for CO_2 electroreduction, CO_2 bubble adhesion to E-MoS_2 and H-E-MoS_2 were measured underwater. The hydrophobic H-E-MoS_2 surface showed more affinity for CO_2 gas than did the E-MoS_2 surface, as shown in Figure S15 of the Supporting Information. E-MoS_2 might impede the process of CO_2 gas diffusion due to its superaerophobicity, causing a weak interaction between CO_2 molecules

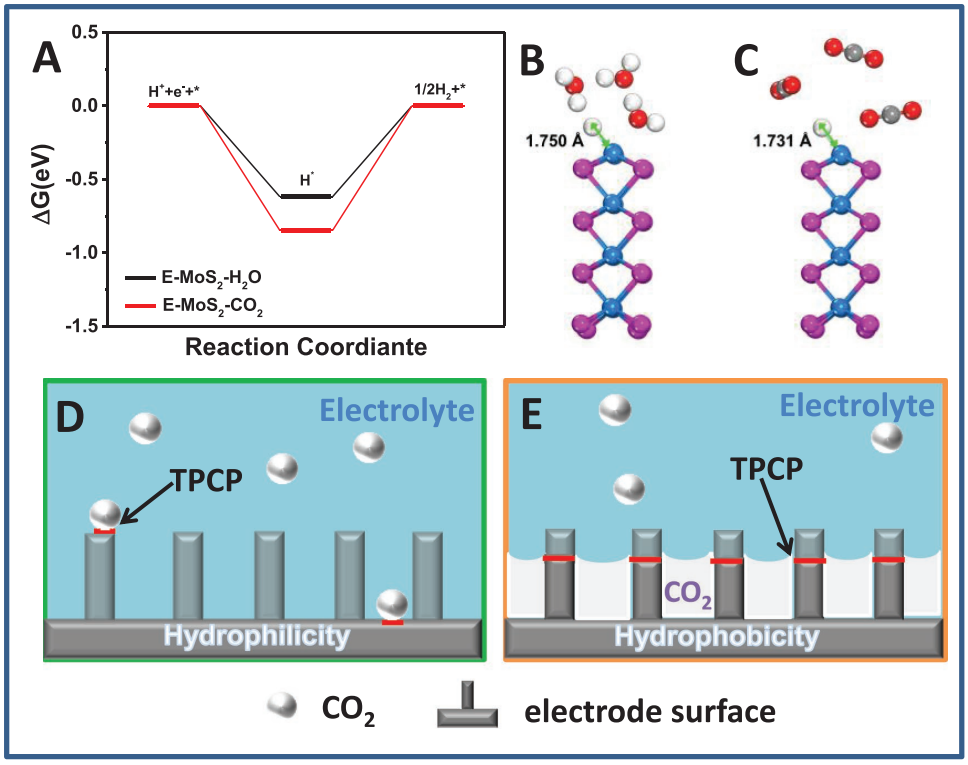

Figure 6. A) Calculated free energy changes for the HER on the E-MoS_2 monolayers under an H_2O environment (black line) and CO_2 environment (red line). Optimized geometries of the H* intermediate on the E-MoS_2 monolayers under B) an H_2O environment and C) a CO_2 environment (H—Mo bond lengths are in Å). D) A thin layer of E-MoS_2 film is immobilized on a GC electrode substrate that appears hydrophilic and aerophobic. When the electrode is immersed in electrolyte solution, the catalyst can only contact the few CO_2 molecules that dissolve in the electrolyte. The red line illustrates the liquid (electrolyte)/gas (CO_2)/solid (electrode) contact point (TPCP) where electron transfer happens. E) After the wettability regulation, an H-E-MoS_2 film is immobilized on the GC electrode substrate, which becomes hydrophobic and aerophilic. Due to the existence of triphase interface, the catalyst can contact much CO_2, which is derived from both the electrolyte and catalyst surface.

and the electrode (Figure 6D). It has been reported previously that hydrophobic residues have the ability to absorb and host the reactant gas to enhance the extent of reaction at the gas–solid–liquid interface.[13,28] Therefore, the H-E-MoS_2 electrode has a hydrophobic and aerophilic surface, in which more CO_2 molecules diffused into the electrolyte due to the abundant three-phase contact point (TPCP) on the electrode (Figure 6E), which led to there being more CO_2 molecules at the gas-solid-liquid interface, and then enhancing the reactivity of CO_2RR. This is the first analysis of the mechanism for the electroreduction of CO_2 to syngas on an FAS-modified electrode by DFT calculations.

3. Conclusions

In summary, an E-MoS_2 dispersion with a large volume and high concentration has been fabricated by a cost-efficient process of wet ball milling. The H-E-MoS_2 nanosheet electrode for CO_2 electroreduction was fabricated by a facile refloating of MoS_2 nanosheets on a glassy carbon electrode, followed by decoration of FAS. H-E-MoS_2 nanosheets, with their hydrophobicity, exhibited a superior CO_2RR performance with a high current density of 61 mA cm^{-2} at –1.1 V, ≈1.25 times higher than that of E-MoS_2. The CO/H_2 ratios of syngas on the H-E-MoS_2 electrode were broadened from 1:2 to 4:1 at a wider range of potentials, compared to those of the E-MoS_2 electrode. In addition, H-E-MoS_2 attained the highest FE of 81.2% for CO production at –0.9 V. Note that HER performance could be obviously suppressed, but CO_2RR activity was enhanced on the H-E-MoS_2 electrode. We proposed that the hydrophobicity of the electrode provided an abundant TPCP for accelerating CO_2 diffusion into electrode, which enhanced CO_2RR performance. Our experimental results were further verified by DFT calculations. The DFT results showed that the FAS decoration of H-E-MoS_2 changed the electric properties of the MoS_2 layer, decreased the energy barrier of the rate-determining CO-desorption step, which thereby promoted CO_2 reduction to produce CO. Furthermore, DFT calculations of hydrophilic E-MoS_2 and hydrophobic H-E-MoS_2 electrodes also found that the CO_2 environment of hydrophobic MoS_2 increased the energy barrier of H desorption, thus suppressing HER. The method used here may provide an effective and facile method for the electrochemical conversion of CO_2 to syngas with a wide range of CO/H_2 ratios by tuning the wettability of the electrode.

4. Experimental Section

Materials: Molybdenum (IV) sulfide powder (MoS_2, CAS: 1317-33-5) was supplied by Sigma-Aldrich. NVP (CAS: 88-12-0) was purchased

from Shanghai Macklin Biochemical Co. Ltd. Trimethoxy (1H,1H,2H,2H-heptadecafluorodecyl) Silane (FAS, CAS: 83048-65-1) was purchased from Alfa Aesar. 1-Ethyl-3-methylimidazolium tetrafluoroborate (EMIM-BF4, CAS: 143314-16-3) was supplied by Shanghai Cheng Jie Chemical Co. LTD. All reagents were used without further treatment.

The Exfoliated MoS_2 (E-MoS_2) Nanosheets: Here, the solvent NVP was used to disperse MoS_2 nanosheets because they have similar surface energies. First, the MoS_2 nanosheet dispersion was prepared according to the reported literature.[16] In a typical experiment, the required mass of MoS_2 powder and ZrO_2 balls (1:1 mass ratio of 2 mm ball and 0.2 mm ball) were added to the jar. The NVP solvent was then added into the jar, in which the concentration of MoS_2 powder was 16 mg mL^{-1}, and the solution was ground for 18 h. The dark green colored dispersion was collected and centrifuged at 550 rpm (centrifugation force 30 N) for 45 min to remove any unexfoliated MoS_2. The dark green colored supernatant was decanted and retained for analysis and further experiments, while the sediment was discarded. To calculate the concentration of the exfoliated MoS_2 (E-MoS_2) nanosheets, the dispersion was filtered using a polytetrafluoroethylene membrane (pore size: 0.1 μm) and the MoS_2 membrane was dried at 60 °C under vacuum for 3 days. The as-prepared E-MoS_2 dispersion was injected into water to form a uniform E-MoS_2 film on the surface of the water. Then, a GC slice (3 cm × 1 cm) was inserted below the surface of water, then slowly drawn and dried for 24 h to obtain an E-MoS_2-coated electrode with 9 mg cm^{-2} of E-MoS_2 nanosheets on it, which was used as the working electrode.

The Hydrophobic E-MoS_2 Nanosheet (H-E-MoS_2) Electrode: E-MoS_2 substrates were treated with air plasma with 2 min (10.5 W) in order to introduce hydrophilic functional groups. Trimethoxy (1H,1H,2H,2H-heptadecafluorodecyl) silane (FAS) was used as the chemical vapor deposition material for the hydrophobic treatment, which was carried out in a beaker that contained liquid FAS in equilibrium with its vapor. The E-MoS_2 electrode was exposed to FAS vapor for 18 h at room temperature to get the hydrophobic and aerophilic E-MoS_2 electrode (denoted as an H-E-MoS_2 electrode).

Characterization: The surface morphology and corresponding elemental mapping analysis of samples were observed by environmental SEM (JEOL, JSM-7500F, Japan). The microstructure and lattice structure of samples were observed by HRTEM (JEOL, JEM-2100F, Japan). The topology of the surface was studied by AFM (VT STM/AFM, Germany) using a Veeco DI Nano-scope MultiMode V system. XRD patterns were obtained with a Shimadzu X-ray diffractometer (XRD-6000) equipped with a Cu-Kα1 source (λ = 1.5406 Å). XPS was performed with Al Kα radiation (Thermo Fisher Scientific, ESCALAB 250Xi, America). Raman spectra were analyzed using 532 nm laser excitation by a Raman spectroscope (LabRAM HR800). A plasma cleaning machine (PDC-32G-2) was equipped with three power settings (low: 6.8 W, medium: 10.5 W, high: 18 W).

Supporting Information

Supporting Information is available from the Wiley Online Library or from the author.

Acknowledgements

The work was supported by the National Natural Science Foundation of China (51672019 and 51473008), the National Key Research and Development Program of China (2017YFA0206902), and the 111 Project (B14009).

Conflict of Interest

The authors declare no conflict of interest.

Keywords

CO_2 electroreduction, exfoliated MoS_2 nanosheets, FAS, hydrophobic electrodes, syngas

Received: April 5, 2018
Revised: June 11, 2018
Published online:

[1] L. Zhong, F. Yu, Y. An, Y. Zhao, Y. Sun, Z. Li, T. Lin, Y. Lin, X. Qi, Y. Dai, *Nature* **2016**, *538*, 84.
[2] P. Su, K. Iwase, S. Nakanishi, K. Hashimoto, K. Kamiya, *Small* **2016**, *12*, 6083.
[3] S. Zhang, P. Kang, S. Ubnoske, M. K. Brennaman, N. Song, R. L. House, J. T. Glass, T. J. Meyer, *J. Am. Chem. Soc.* **2014**, *136*, 7845.
[4] F. Jiao, J. Li, X. Pan, J. Xiao, H. Li, H. Ma, M. Wei, Y. Pan, Z. Zhou, M. Li, *Science* **2016**, *351*, 106.
[5] W. Sheng, S. Kattel, S. Yao, B. Yan, Z. Liang, C. Hawxhurst, Q. Wu, J. G. Chen, *Energy Environ. Sci.* **2017**, *10*, 1180.
[6] R. He, A. Zhang, Y. Ding, T. Kong, Q. Xiao, H. Li, Y. Liu, J. Zeng, *Adv. Mater.* **2018**, *30*, 1705872.
[7] L. Dai, Q. Qin, P. Wang, X. Zhao, C. Hu, P. Liu, R. Qin, M. Chen, D. Ou, C. Xu, S. Mo, B. Wu, G. Fu, P. Zhang, N. Zheng, *Sci Adv.* **2017**, *3*, e1701069.
[8] Y. Li, H. Wang, L. Xie, Y. Liang, G. Hong, H. Dai, *J. Amer. Chem. Soc.* **2011**, *133*, 7296.
[9] M. Asadi, B. Kumar, A. Behranginia, B. A. Rosen, A. Baskin, N. Repnin, D. Pisasale, P. Phillips, W. Zhu, R. Haasch, *Nat. Commun.* **2014**, *5*, 4470.
[10] P. Abbasi, M. Asadi, L. Cong, S. Sharifiasl, B. Sayahpour, A. Behranginia, P. Zapol, R. Shahbazianyassar, L. A. Curtiss, A. Salehikhojin, *ACS Nano* **2016**, *11*, 453.
[11] L. Yu, Y. Xie, J. Zhou, Y. Li, Y. Yu, Z. Ren, *J. Mater. Chem. A* **2018**, *6*, 4706.
[12] F. Li, S. F. Zhao, L. Chen, A. Khan, D. R. Macfarlane, J. Zhang, *Energy Environ. Sci.* **2016**, *9*, 216.
[13] J. Xu, X. Li, W. Liu, Y. Sun, Z. Ju, T. Yao, C. Wang, H. Ju, J. Zhu, S. Wei, Y Xie, *Angew. Chem., Int. Ed.* **2017**, *56*, 9121.
[14] C. Teng, D. Xie, J. Wang, Z. Yang, G. Ren, Y. Zhu, *Adv. Funct. Mater.* **2017**, *27*, 20.
[15] J. N. Coleman, V. Nicolosi, *Science* **2011**, *42*, 568.
[16] E. Varrla, C. Backes, K. R. Paton, A. Harvey, Z. Gholamvand, J. Mccauley, J. N. Coleman, *Chem. Mater.* **2015**, *17*, 1129.
[17] L. Yin, X. Hai, K. Chang, F. Ichihara, J. Ye, *Small* **2018**, *14*, 1704153.
[18] A. O'Neill, U. Khan, J. N. Coleman, *Chem. Mater.* **2012**, *24*, 2414.
[19] R. J. Smith, P. J. King, M. Lotya, C. Wirtz, U. Khan, S. De, A. O'Neill, G. S. Duesberg, J. C. Grunlan, G. Moriarty, *Adv. Mater.* **2011**, *23*, 3944.
[20] K. G. Zhou, N. N. Mao, H. X. Wang, Y. Peng, H. L. Zhang, *Angew. Chem., Int. Ed.* **2011**, *50*, 10839.
[21] J. N. Coleman, M. Lotya, A. O'Neill, S. D. Bergin, P. J. King, U. Khan, K. Young, A. Gaucher, S. De, R. J. Smith, *Science* **2011**, *331*, 568.
[22] Y. Yao, Z. Lin, Z. Li, X. Song, K. S. Moon, C. Wong, *J. Mater. Chem.* **2012**, *22*, 13494.
[23] Y. Qi, N. Wang, Q. Xu, H. Li, P. Zhou, X. Lu, G. Zhao, *Chem. Commun.* **2015**, *51*, 6726.
[24] S. S. Chou, N. Sai, P. Lu, E. N. Coker, S. Liu, K. Artyushkova, T. S. Luk, B. Kaehr, C. J. Brinker, *Nat. Commun.* **2015**, *6*, 8311.
[25] M. A. Lukowski, A. S. Daniel, F. Meng, A. Forticaux, L. Li, S. Jin, *J. Am. Chem. Soc.* **2013**, *135*, 10274.

[26] H. Li, Q. Zhang, C. C. R. Yap, B. K. Tay, T. H. T. Edwin, A. Olivier, D. Baillargeat, *Adv. Funct. Mater.* **2012**, *22*, 1385.
[27] D. Voiry, M. Salehi, R. Silva, T. Fujita, M. Chen, T. Asefa, V. B. Shenoy, G. Eda, M. Chhowalla, *Nano Lett.* **2013**, *13*, 6222.
[28] C. Zhao, X. Dai, T. Yao, W. Chen, X. Wang, J. Wang, J. Yang, S. Wei, Y. Wu, Y. Li, *J. Am. Chem. Soc.* **2017**, *139*, 8078.
[29] C. Tsai, F. Abildpedersen, J. K. Nørskov, *Nano Lett.* **2014**, *14*, 1381.
[30] Y. Lei, R. Sun, X. Zhang, X. Feng, L. Jiang, *Adv. Mater.* **2016**, *28*, 1477.
[31] X. Wang, C. Zhao, X. Zhao, Y. Tao, W. Chen, Y. Rui, C. Zhao, W. Geng, W. Jing, W. Huang, *Angew. Chem., Int. Ed.* **2018**, *130*, 1962.
[32] M. Asadi, K. Kim, C. Liu, A. V. Addepalli, P. Abbasi, P. Yasaei, P. Phillips, A. Behranginia, J. M. Cerrato, R. Haasch, *Science* **2016**, *353*, 467.
[33] J. Xie, X. Zhao, M. Wu, Q. Li, Y. Wang, J. Yao, *Angew. Chem., Int. Ed.* **2018**, *57*, https://doi.org/10.1002/anie.201802055.